Journal of Alloys and Compounds 675 (2016) 223–230

Contents lists available at ScienceDirect

Journal of Alloys and Compounds

journal homepage: http://www.elsevier.com/locate/jalcom

A comparative study on the isochronal and isothermal crystallization kinetics of $Co_{46.45}Fe_{25.55}Ta_8B_{20}$ soft magnetic metallic glass with high thermal stability

Amir Hossein Taghvaei [a, *], Jürgen Eckert [b, c]

[a] Department of Materials Science and Engineering, Shiraz University of Technology, Shiraz, Iran
[b] Erich Schmid Institute of Materials Science, Austrian Academy of Sciences, Jahnstraße 12, A-8700 Leoben, Austria
[c] Department Materials Physics, Montanuniversität Leoben, Jahnstraße 12, A-8700 Leoben, Austria

ARTICLE INFO

Article history:
Received 22 October 2015
Received in revised form
19 February 2016
Accepted 9 March 2016
Available online 10 March 2016

Keywords:
Metallic glass
Crystal growth
Diffusion
Kinetics

ABSTRACT

The crystallization kinetics of $Co_{46.45}Fe_{25.55}Ta_8B_{20}$ soft magnetic metallic glass with high thermal stability has been systematically investigated during isochronal and isothermal annealing treatments. The kinetics parameters have been calculated using different approaches, such as Kissinger, Ozawa, Augis–Bennett, Gao and Johnson-Mehl-Avrami (JMA) for isochronal crystallization and JMA for the isothermal regime. According to the isoconversional approach, it has been shown that the nucleation of the $(Co,Fe)_{21}Ta_2B_6$ phase during continuous heating needs a higher energy barrier compared to its growth, where the average activation energy value is smaller than the apparent one. The Avrami exponent values for isochronal crystallization at all heating rates, calculated according to the Gao model, shows a good agreement with those determined by the JMA model at the beginning of crystallization. The JMA model demonstrates that the average Avrami exponent is around 2 for isochronal crystallization, revealing a three-dimensional diffusion-controlled crystal growth with a decreasing nucleation rate. It has been shown that based on the JMA model, the site saturation occurs for crystallized fraction (α) beyond 0.3 in the isochronal condition, so that the normal grain growth (NGG) model with an exponent of 0.32 can be applied for $\alpha \geq 0.5$. The results manifest that the average Avrami exponent and the overall nucleation rate of $(Co,Fe)_{21}Ta_2B_6$ crystals in the isothermal and isochronal conditions are comparable and the nucleation process occurs over a notably larger crystallized fraction in the isothermal condition.

1. Introduction

Metallic glasses (MGs) are metastable materials with improved physical, chemical and mechanical properties, compared to their crystalline counterparts. The absence of lattice periodicity and crystalline defects in MGs can result in good corrosion resistance, high fracture strength and hardness, low elastic modulus and excellent soft magnetic properties, making MGs promising for many industrial applications [1–8]. Due to the metastable nature of MGs, a decrease in their free energy and their transformation to more stable states are possible during heating, as a result of crystallization [1]. It is well-known that many physical and mechanical properties of MGs can significantly change upon (partial) devitrification [9–11]. For example, several studies have indicated that the controlled formation of nanocrystals in an amorphous matrix during heating of some Fe-based MGs can drastically improve their magnetic properties [12,13]. Moreover, a noticeable enhancement in strength and toughness has been obtained in some Al-Ni-based amorphous alloys by partial crystallization via the development of ductile crystals in the amorphous matrix [14]. Hence, it is of great importance to gain knowledge about the kinetics of crystallization, i.e., the nucleation and growth behaviors of crystalline phases during heating of MGs. In addition, the investigation of the crystallization kinetics and the calculation of thermal parameters give valuable information about the thermal stability of MGs. It is known that thermal stability plays a leasing role in determining the suitable temperature and time for the thermo-mechanical treatment of MGs in the temperature range of supercooled liquid region (SLR) [1,15,16].

In general, the crystallization kinetics of a MG can be studied in

* Corresponding author.
E-mail address: amirtaghvaei@gmail.com (A.H. Taghvaei).

http://dx.doi.org/10.1016/j.jallcom.2016.03.053
0925-8388/

either isothermal or isochronal heating experiments. In the case of isothermal crystallization, a MG is heated up to a temperature in the SLR and held for a certain period of time for crystallization. The kinetics of isothermal crystallization can be studied by the well-known Johnson-Mehl-Avrami (JMA) approach [17,18]. However, in isochronal crystallization, a MG is heated continuously above the crystallization temperature at a certain heating rate. Compared to the isothermal experiments, non-isothermal heating is more interesting because it can be carried out faster even beyond the temperature range accessible for the isothermal condition [19]. Kinetics parameters in isochronal crystallization can be determined by using different approaches suggested by Kissinger [20], Ozawa [21], JMA [18], Augis–Bennett [22], Gao [23] and Kempen [24]. Many studies have shown that the crystallization behavior and corresponding kinetic parameters can be different for a MG heated in isochronal and isothermal conditions [25–27].

In the present paper, the crystallization kinetics of $Co_{46.45}Fe_{25.55}Ta_8B_{20}$ MG was systematically investigated in both isochronal and isothermal heating regimes. Our previous work indicated that the $Co_{46.45}Fe_{25.55}Ta_8B_{20}$ MG exhibits a wide SLR of 51 K, demonstrating a high thermal stability [28]. Furthermore, it was shown that this alloy offers promising soft magnetic properties, including a high saturation magnetization of 93.5 Am^2/kg and a very low coercivity of 1.2 A/m [28]. The activation energy of crystallization in the isochronal condition was calculated and compared by using the Kissinger, Ozawa, Augis–Bennett and Gao approaches. The crystallization mechanism upon isochronal heating was discussed based on overall and local kinetics parameters calculated by using the Gao and JMA approaches. In addition, the JMA model was applied for isothermal crystallization in order to evaluate and compare the activation energy, nucleation and growth behaviors of crystals with those of isochronal heating.

2. Experimental procedure

$Co_{46.45}Fe_{25.55}Ta_8B_{20}$ master alloy was obtained by arc-melting of pure Co (99.9%), Fe (99.9%), Ta (99.96%) and crystalline B (99.5%). In order to increase the chemical homogeneity, the alloy ingot was re-melted at least three times under a Ti-gettered Ar atmosphere. A single-roller Bühler melt-spinner was employed to produce glassy ribbons with 2 mm of width and 30 μm of thickness under an Ar atmosphere. The rotation speed of the copper wheel was selected as 41 m/s.

The phase analysis of the ribbons was conducted by X-ray diffraction (XRD) in a reflection mode by using CoK_α radiation with a corresponding wave length of $\lambda = 1.7902$ Å. The thermal behavior and crystallization kinetics under continues heating at different heating rates (10–40 K/min) were examined by using a differential scanning calorimeter (DSC, NETZSCH DSC 404) working under a flow of purified Ar. The isothermal crystallization behavior at different temperatures was evaluated by a Perkin–Elmer DSC7 under a continuous flow of high-purity Ar.

3. Results and discussion

3.1. Isochronal crystallization kinetics

The heating rate dependence of glass transition temperature (T_g), onset temperature (T_x) and peak temperature (T_p) of the first crystallization event was investigated in the previous work [28]. The apparent activation energy of the first crystallization event (E_c) was calculated based on the Kissinger and Ozawa methods, as listed in Table 1. As well as these approaches, E_c can be determined by other equations suggested by Augis–Bennett [22] and Gao et al. [23]. In the Augis–Bennett equation, E_c can be calculated as [22]:

Table 1
Apparent activation energy of the first crystallization event (E_c) of the $Co_{46.45}Fe_{25.55}Ta_8B_{30}$ MG calculated by the different models.

Models	Kissinger	Ozawa	Augis–Bennett	Gao
E_c (kJ/mol)	445 ± 11 [24]	438 ± 10 [24]	453 ± 10	420 ± 25

$$\ln\frac{T_p}{\beta} = \frac{E_c}{RT_p} + \ln K_0, \tag{1}$$

where β is the heating rate, R is the gas constant and K_0 is the pre-exponential factor. Fig. 1 depicts the variation of lnT_p/β as a function of $1000/T_p$, indicating a straight line with a slope of 453 ± 5 kJ/mol corresponding to E_c, which shows a good agreement with the values reported in Table 1. Moreover, Gao et al. [23] derived an equation from the JMA approach in order to calculate E_c from variations in the maximum transformation rate with T_p, according to the following relation:

$$\ln\left(\frac{d\alpha}{dt}\right)_p = -\frac{E_c}{RT_p} + c, \tag{2}$$

where α is the crystallized fraction, $(d\alpha/dt)_p$ is the rate of crystallization at T_p and c is a constant. The crystallized fraction, α, at each heating rate can be obtained as:

$$\alpha = \frac{A_x}{A_\infty}, \tag{3}$$

where A_∞ is the total area of the crystallization event and A_x is the partial area between T_x and any given temperature T ranging between T_x andT_∞. Before the integration, the contribution of the heat capacity changes upon crystallization was subtracted from the total heat released by an iterative procedure [29].

Fig. 2 depicts the evolution of α as a function of temperature for different heating rates. It is observed that all of the curves show a sigmoid type with slow crystallization rates at the beginning and end of crystallization, which is typical for devitrification of metallic glasses [26,30]. Initially, nucleation takes place at different points in the bulk of the samples, i.e. bulk crystallization becomes dominant. As the surface area of nucleation increases, the growth of the nuclei

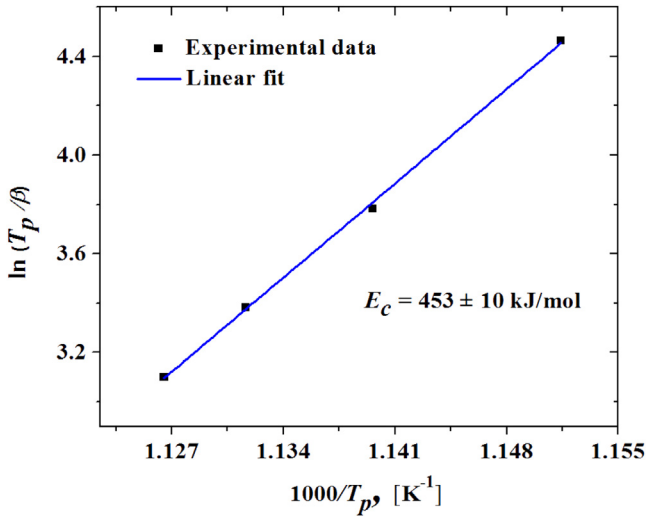

Fig. 1. Augis–Bennett plot for the calculation of the apparent activation energy of the first crystallization event (E_c) of the $Co_{46.45}Fe_{25.55}Ta_8B_{30}$ MG.

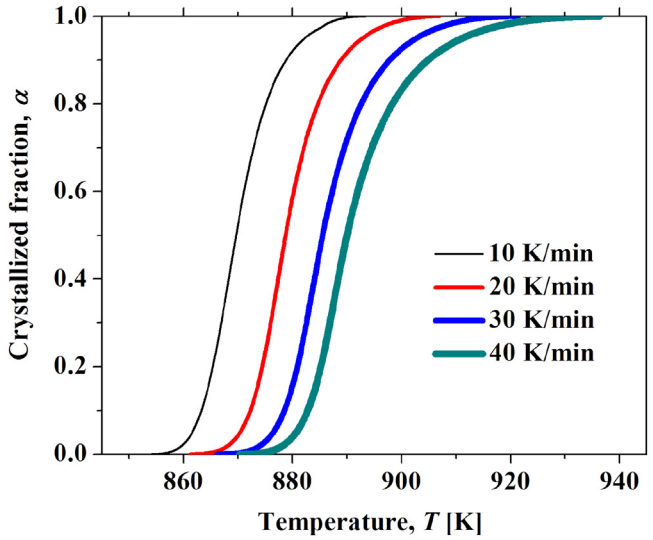

Fig. 2. Evolution of the crystallized fraction (α) versus temperature, determined for the first crystallization event of the $Co_{46.45}Fe_{25.55}Ta_8B_{30}$ MG at the different heating rates.

occurs with a rapid reaction rate. Finally, due to the impingement of crystals and the decrease in the surface area of nucleation, the crystallization rate decreases. The evolution of $(d\alpha/dt)$ as a function of temperature, calculated at the different heating rates, is shown in Fig. 3(a). For each heating rate, it can be seen that $(d\alpha/dt)$ shows a maximum value at a temperature corresponding to T_p, which signifies the maximum crystallization rate. The variation of $ln(d\alpha/dt)_p$ with respect to $1000/T_p$ is shown in Fig. 3(b). As the figure shows, the least-square fitting of the data point results in an straight line with a slope of 420 ± 25 kJ/mol, assigned to E_c, which shows a relatively good agreement with the values listed in Table 1. In addition to E_c, it is worth to note that the approach suggested by Gao et al. [23] can be used in order to evaluate other important kinetics parameters like the maximum transformation rate constant, K_p, and the Avrami exponent, n, as [23]:

$$\left(\frac{df}{dt}\right)_p = 0.37nK_p, \tag{4}$$

$$K_p = \frac{\beta E_c}{RT_p^2}, \tag{5}$$

Table 2 lists the values of $(d\alpha/dt)_p$, K_p and n for the $Co_{46.45}Fe_{25.55}Ta_8B_{20}$ MG at the different heating rates. It can be seen that n values are almost identical and do not show any heating rate dependency, which is in line with the isokinetics assumption of the phase transformation [31]. It is known that the Avrami exponent n can reflect the mechanisms of nucleation and growth during phase transformations, which can be written as [32]:

$$n = b + pm \tag{6}$$

where b denotes the index for nucleation ($b = 0$ for the zero nucleation rate, $0 < b < 1$ for a decreasing nucleation rate, $b = 1$ for a constant nucleation rate and $b > 1$ for an increasing nucleation rate), p is the growth index ($p = 0.5$ for diffusion-controlled growth and $p = 1$ for interface-controlled growth), and m is the dimensionality of growth ($m = 1$, 2 and 3 for one-, two- and three-dimensional growths, respectively). According to Table 2, the n values are close to 3. Based on Eq. (6), this value indicates that the crystallization occurs through a three-dimensional interface-controlled growth of quenched-in nuclei (site saturation) or a three-dimensional interfaced-controlled growth with an increasing nucleation rate. It should be noted that the absence of pre-existing nuclei in the $Co_{46.45}Fe_{25.55}Ta_8B_{20}$ MG was confirmed by transmission electron microscopy (not shown here). As a result, based on the above kinetics model, the $(Co,Fe)_{21}Ta_2B_6$ crystals are formed upon isochronal heating by a three-dimensional diffusion-

Table 2
Gao kinetics parameters at the different heating rates, corresponding to the first crystallization reaction of the $Co_{46.45}Fe_{25.55}Ta_8B_{30}$ MG. $(d\alpha/dT)_p$ is the maximum crystallization rate, K_p is the maximum reaction rate constant, and n is the Avrami exponent.

Heating rate (K/min)	$(d\alpha/dT)_p$ (1/min)	K_p (1/min)	n
10	0.75	0.67	3
20	1.50	1.32	3
30	2.07	1.95	2.9
40	2.68	2.56	2.8

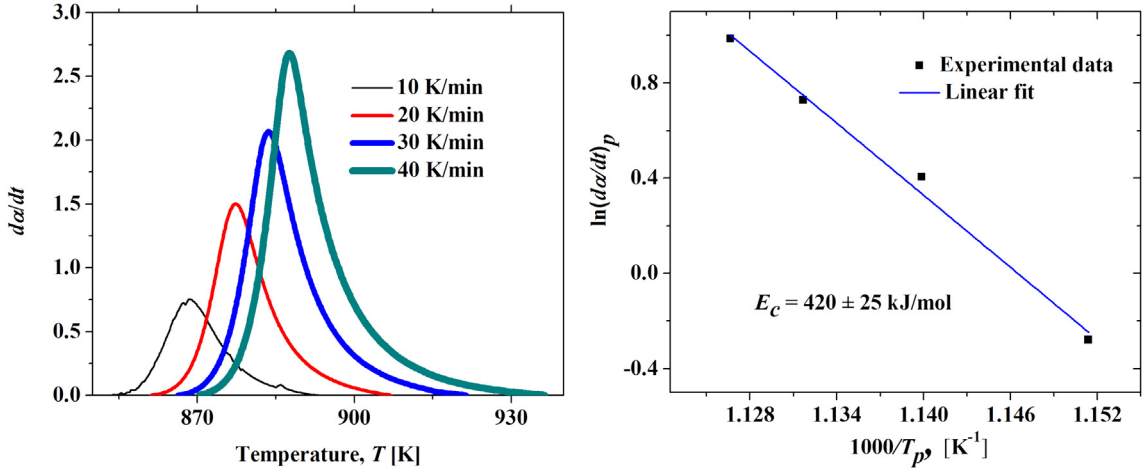

Fig. 3. Variations of the first crystallization rate of the $Co_{46.45}Fe_{25.55}Ta_8B_{30}$ MG versus temperature at different heating rates (a) and Gao plots for the calculation of the apparent activation energy of the first crystallization event (E_c) (b).

controlled growth with an increasing nucleation frequency.

The crystallization activation energies listed in Table 1 demonstrate the overall or effective energy barrier for nucleation and subsequent growth of nuclei. The kinetics parameters are not usually constant during the progress of crystallization, as a result of ongoing changes in the mechanism and contributions of the nucleation and growth phenomena. Hence, the local kinetics parameters can be deviated from a constant value and exhibit a dependency on the crystallized fraction. According to the isoconversional approach [33], the local energy barrier of crystallization $E_c(\alpha)$ can be determined based on a relation similar to the Ozawa equation as [21]:

$$\ln \beta = -1.0516\frac{E_c(\alpha)}{RT_\alpha} + C, \tag{8}$$

where T_α is the temperature corresponding to a certain crystallized fraction α, which can be obtained from Fig. 2.

The evolution of $E_c(\alpha)$ as a function of the devitrified fraction α (Fig. 4) manifests that the crystallization energy barrier exhibits a strong dependence on α. As the figure shows, $E_c(\alpha)$ initially decreases from 445 kJ/mol at $\alpha = 0.02$–426 kJ/mol at $\alpha = 0.1$. It remains relatively unchanged up to $\alpha = 0.5$ and then decreases gradually up to the end of the first crystallization event. According to Fig. 4, the average activation energy of crystallization is 400 kJ/mol, which is slightly lower than the apparent ones listed in Table 1. It is worth noting that the fraction dependence of $E_c(\alpha)$ for the present MG is completely different compared to that of the $Co_{40}Fe_{22}Ta_8B_{30}$ MG, which indicates an increasing trend for $E_c(\alpha)$ with α [33]. In the case of the $Co_{46.45}Fe_{25.55}Ta_8B_{20}$ MG, only the face-centered cubic (FCC) $(Co,Fe)_{21}Ta_2B_6$ phase is formed upon primary crystallization [28]. However, it was shown that the primary crystallization event of the $Co_{40}Fe_{22}Ta_8B_{30}$ MG resulted in the formation of the $(Co,Fe)_{21}Ta_2B_6$ phase as well as a small amount of the $(Co,Fe)_3B_2$ crystals, which in turn causes a different evolution of $E_c(\alpha)$ with α [33].

During the isochronal crystallization of a MG, it has been suggested that nucleation takes place only at the early stage of the transformation, and the grain growth phenomenon is expected to be dominant in the rest of devitrification [34]. This effect implies that the $E_c(\alpha)$ values calculated at small α values are mainly attributed to the energy barrier required for nucleation (E_n). In the same way, the values of $E_c(\alpha)$ at the final stage of crystallization dominantly shows the essential energy barrier for the growth of the precipitated nuclei (E_g). $E_c(\alpha)$ at other α values includes both E_n and E_g, with different contributions depending on the local Avrami exponent values [35]. According to Fig. 4, E_n and E_g for the $Co_{46.45}Fe_{25.55}Ta_8B_{20}$ MG are about 445 and 318 kJ/mol, respectively. It is observed that the $Co_{46.45}Fe_{25.55}Ta_8B_{20}$ MG exhibits a higher energy barrier for the nucleation of the $(Co,Fe)_{21}Ta_2B_6$ phase compared to its growth. It has been demonstrated that in metal-boron amorphous alloys, a network-like medium-range ordering can be created through the connection of the boron-centered tri-capped trigonal prism (TTP) type polyhedra with a different atomic structure compared to the $(Co,Fe)_{21}Ta_2B_6$ phase [28]. Hence, formation of the $(Co,Fe)_{21}Ta_2B_6$ phase requires a drastic atomic rearrangement and long-range diffusion of the constituent elements, which is consistent with a higher activation energy for nucleation and the wide SLR of this alloy (51 K) [28]. On the other hand, after the nucleation of the $(Co,Fe)_{21}Ta_2B_6$ phase, the chemical composition of the remaining amorphous matrix is probably changed, which results in different activation energy values for growth of the $(Co,Fe)_{21}Ta_2B_6$ crystals.

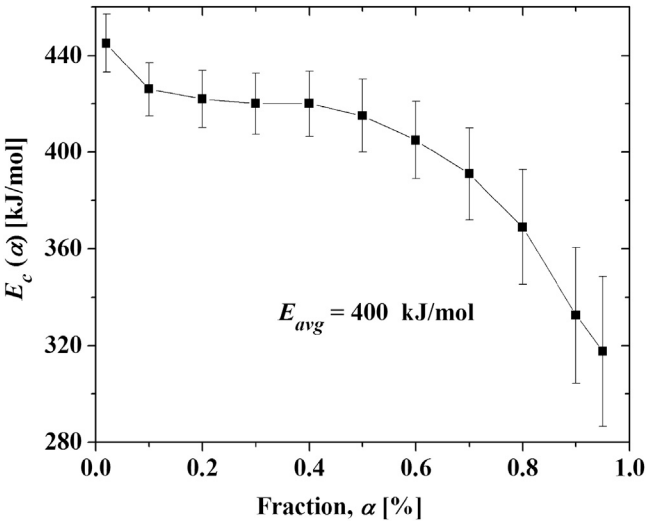

Fig. 4. Variations of the local activation energy of the first crystallization event ($E_c(\alpha)$) of the $Co_{46.45}Fe_{25.55}Ta_8B_{30}$ MG versus crystallized fraction (α), calculated in the isochronal condition.

As well as the activation energy, the Avrami exponent n can have local values and change as crystallization proceeds due to the variations expected in the nucleation or growth mechanism. To calculate the local values of n, the JMA approach can be used, provided that total nucleation takes place at the initial stage of the process, then growth only becomes dominant and the crystals are uniformly participated in the amorphous matrix [18,36]. In this case, the transformation rate is given by Ref. [36]:

$$\frac{d\alpha}{dt} = f(\alpha)K(T), \tag{9}$$

where $f(\alpha)$ is a function of the transformed fraction, describing the crystallization mechanism. According to the JMA model which considers both nucleation and growth processes, $f(\alpha)$ is given by Refs. [18,37]:

$$f(\alpha) = n(1-\alpha)[-\ln(1-\alpha)]^{\frac{n-1}{n}}, \tag{10}$$

While for the model describing only the normal grain growth (NGG) of the precipitated nuclei, $f(\alpha)$ is calculated as [38]:

$$f(\alpha) = (1-\alpha)^{m+1}, \tag{11}$$

In Eq. (9), $K(T)$ is the reaction rate constant given by Refs. [18,37]:

$$K(T) = A_0 \exp\left(-\frac{E_c}{RT}\right), \tag{12}$$

where A_0 is the frequency factor. The combination of Eqs. (9) and (12) gives:

$$\ln\left(\frac{d\alpha}{dt}\right) + \frac{E_c}{RT} = \ln(A_0 f(\alpha)), \tag{13}$$

In Eq. (13), the right-hand side changes only with the crystallized fraction and can be calculated from the known values of E_c and $(d\alpha/dt)$ represented in Table 1 and Fig. 3(a), respectively. The values of $ln(d\alpha/dt) + E_c/RT$ ($E_c = 445$ kJ/mol) at the different heating rates were averaged for the same crystallized fraction and were plotted versus $-ln(1-\alpha)$(Fig. 5). It can be observed that $ln(A_0 f(\alpha))$ changes significantly by progression of crystallization, which demonstrates various devitrification mechanisms at the different stages of transformation. According to Fig. 5, $ln(A_0 f(\alpha))$ rapidly increases at

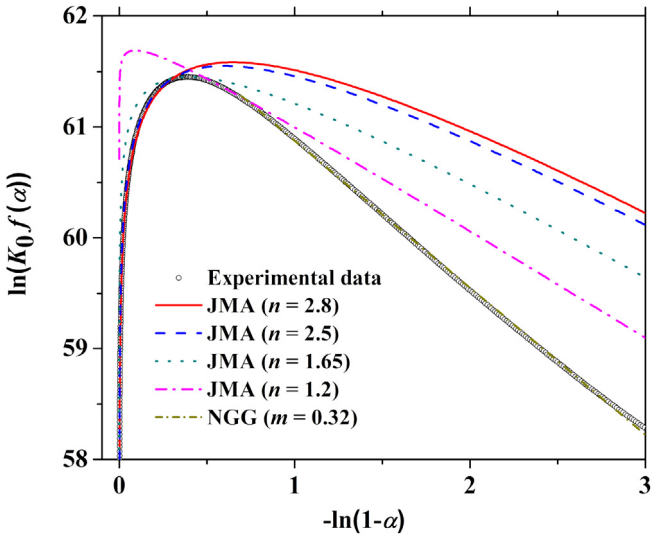

Fig. 5. Evolution of $ln(A_0 f(\alpha))$ as a function of $-ln(1-\alpha)$, calculated from Eq. (13) for the first crystallization event of the $Co_{46.45}Fe_{25.55}Ta_8B_{30}$ MG, and the corresponding kinetics parameters obtained by the different curve fittings according to the JMA and NGG models.

the early transformation stages, reaches a maximum value of 61.45 at $\alpha = 0.32$ and subsequently decreases linearly in the range of $0.50 \leq \alpha \leq 0.95$. It was found that (not shown in the paper) the heating rate has a negligible effect on the trend and evolution of $ln(A_0 f(\alpha))$, which reflects the same kinetics parameters and consequently the similar crystallization mechanisms at each heating rate. This is in good agreement with the isokinetics assumption in the JMA model.

In order to find the kinetics parameters including n, m and A_0 at the different crystallization stages, the least-square minimization curve fitting procedure was performed by comparison of the data point in Fig. 5 with the plot of $ln(f(\alpha))$ as a function of $-ln(1-\alpha)$ determined from Eqs. (10) and (11). As can be inferred from Fig. 5, the JMA model with $\ln A_0 = 61.47$ and $n = 2.8$ can be applied to describe the crystallization kinetics for $\alpha \leq 0.05$. This result indicates that at the beginning of crystallization, a three-dimensional diffusion-controlled growth with increasing nucleation rates is dominant, which is in good agreement with the kinetics results mentioned in Table 2. Furthermore, the JMA model with $\ln A_0 = 61.53$ and $n = 2.5$ shows the best fitting result for $0.05 < \alpha \leq 0.26$, which signifies that the nucleating rate decreases while a diffusion-controlled growth is still taking place. The n value decreases to 1.65 for $0.30 \leq \alpha \leq 0.36$ and $\ln A_0$ increases to 61.7, reflecting a three-dimensional growth with a zero nucleation rate, which is the characteristic of the site saturation. Furthermore, a more decrease in the Avrami exponent up to $n = 1.2$ occurs for $0.39 \leq \alpha \leq 0.5$, and $\ln A_0$ becomes 61.9 for this range. As Fig. 5 shows, by more progression of crystallization, the plot shows a linear behavior, indicating that the NGG model with the exponent of $m = 0.32$ becomes dominant for $0.5 < \alpha \leq 0.95$. The above results confirm that in the case of the isochronal crystallization of the $Co_{46.45}Fe_{25.55}Ta_8B_{20}$ MG, the nucleation rate continuously decreases and crystallization dominantly proceeds by the growth of nuclei precipitated in the initial stages of crystallization ($\alpha \leq 0.3$). According to the above results, the average Avrami exponent for $\alpha \leq 0.5$ is 2, which is lower than those calculated by the Gao model ($n = 3$). Hence, for the $Co_{46.45}Fe_{25.55}Ta_8B_{20}$ MG, it is concluded that the Gao model can give the Avrami exponent for the initial stage of crystallization ($\alpha \leq 0.05$).

3.2. Isothermal crystallization kinetics

In addition to the isochronal crystallization kinetics, the isothermal devitrification kinetics of the $Co_{46.45}Fe_{25.55}Ta_8B_{20}$ MG was studied. For this purpose, the glassy ribbons were heated up to different temperatures in the SLR at a heating rate of 20 K/min, kept for a certain period of time for complete crystallization, and subsequently cooled to room temperature at 100 K/min. Fig. 6 shows the isothermal DSC plots of the $Co_{46.45}Fe_{25.55}Ta_8B_{20}$ ribbon at different annealing temperatures. As can be seen, all of the DSC curves indicate a single exothermic event after a certain incubation period corresponding to the crystallization of the glassy phase. Fig. 7 indicates the XRD patterns of the $Co_{46.45}Fe_{25.55}Ta_8B_{20}$ alloy after the isothermal and isochronal crystallization treatments. For isothermal crystallization, according to Fig. 6, the $Co_{46.45}Fe_{25.55}Ta_8B_{30}$ MG was annealed at 853 K for 20 min. Based on Fig. 7, it is concluded that similar to isochronal crystallization, the isothermal heating process results in the formation of only the $(Co,Fe)_{21}Ta_2B_6$ phase. The average crystallite size, calculated by the Scherer equation [39], for the $(Co,Fe)_{21}Ta_2B_6$ phase precipitated after the isothermal and isochronal heating processes is 57 ± 2 nm and 64 ± 2 nm, respectively.

The evolution of the $(Co,Fe)_{21}Ta_2B_6$ phase fraction as a function of heating time for each annealing temperature was determined by dividing the partial area of each exothermic event up to a certain period to its total area, as shown in Fig. 8. As can be seen, all of the plots exhibit a sigmoid shape, similar to those calculated for isochronal crystallization displayed in Fig. 2. According to Fig. 8, it is obvious that the incubation period decreases and the curves shift to left, manifesting that the crystallization rate increases as a result of the enhanced diffusivity of atoms upon rising temperature.

The crystallization kinetics in the isothermal mode can be investigated by the JMA model, according to the following equation [17,18]:

$$\alpha = 1 - \exp\left[-(K(t-\tau))^n\right], \tag{14}$$

where K is the reaction rate constant (Eq. (12)), α is the transformed fraction at time t and τ is the incubation time. The above equation can be written as:

$$\ln(-\ln(1-\alpha)) = n\ln(t-\tau) + n\ln K, \tag{15}$$

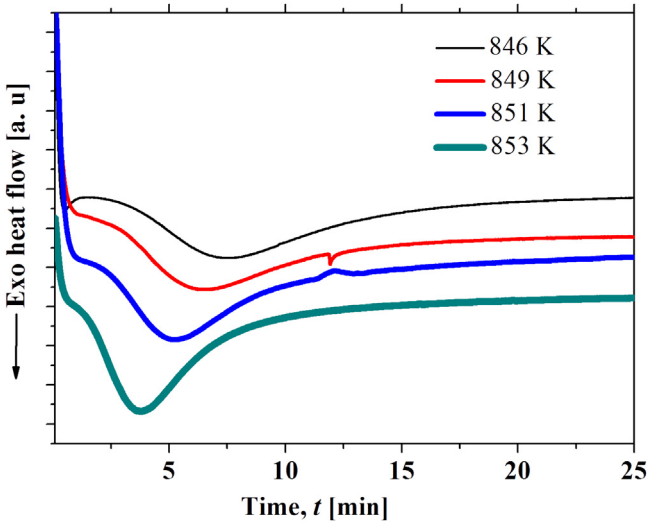

Fig. 6. Isothermal DSC plots of the $Co_{46.45}Fe_{25.55}Ta_8B_{20}$ MG at the different annealing temperatures.

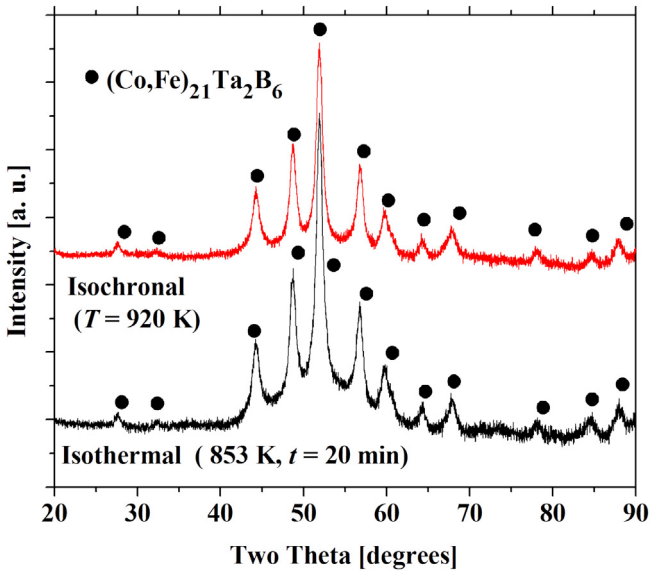

Fig. 7. The XRD patterns of the $Co_{46.45}Fe_{25.55}Ta_8B_{20}$ alloy after crystallization in the isochronal and isothermal conditions.

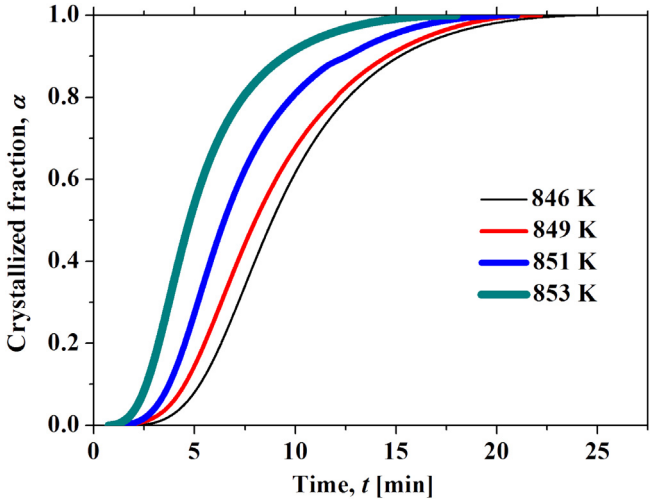

Fig. 8. Evolution of the crystallized fraction in the isothermal condition versus time at the different annealing temperatures, calculated for the $Co_{46.45}Fe_{25.55}Ta_8B_{20}$ MG.

Hence, the kinetics parameters K and n can be obtained by plotting $ln(-ln(1-\alpha))$ versus$ln(t-\tau)$, as depicted in Fig. 9. As the figure shows, the JMA plots are almost linear in the range of $0.01 \leq \alpha \leq 0.63$. Subsequently, their slopes decrease with increasing the crystallized fraction, and a deviation from linearity can be observed for each plots particularly for $\alpha \geq 0.94$. Table 3 lists the values of n at each annealing temperature, as obtained from the linear fitting of the experimental data in Fig. 9 for $0.01 \leq \alpha \leq 0.63$. It is inferred that the Avrami exponent is independent on the annealing temperature and is close to $n = 2.5$, which is the characteristic of a three-dimensional growth with a constant nucleation rate. In addition, such Avrami exponent values are slightly larger than the average value of $n = 2$, obtained from the JMA approach for crystallization in the isochronal mode (Fig. 5). However, since the JMA plots in Fig. 9 exhibit a non-linear behavior for $\alpha > 0.63$, it can be understood that the nucleation or growth behavior may change upon crystallization and can show a dependency on the crystallized

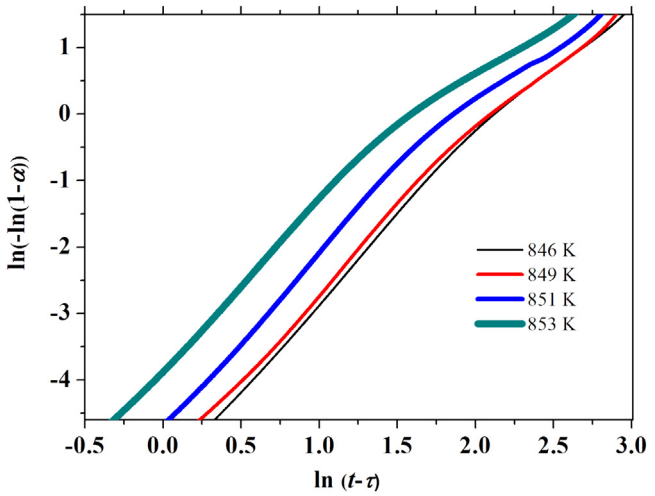

Fig. 9. JMA plots of the $Co_{46.45}Fe_{25.55}Ta_8B_{20}$ MG, determined in the isothermal annealing at the different temperatures.

Table 3
JMA kinetics parameters of the $Co_{46.45}Fe_{25.55}Ta_8B_{30}$ MG, calculated upon isothermal crystallization at the different annealing temperatures. n is the Avrami exponent and n_{avg} is the average Avrami exponent.

Temperature (K)	n	n_{avg}
846	2.63	2.07
849	2.58	2.10
851	2.61	1.90
853	2.49	1.75

fraction. In this case, the local Avrami exponent may offer more realistic results to determine the crystallization kinetics. According to Eq. (15), the local Avrami exponent $n(\alpha)$ at the different stages of crystallization is calculated as:

$$n(\alpha) = \frac{d\ln(-\ln(1-\alpha))}{d\ln(t-\tau)}, \tag{16}$$

Fig. 10 depicts the variations of $n(\alpha)$ versus α for the different

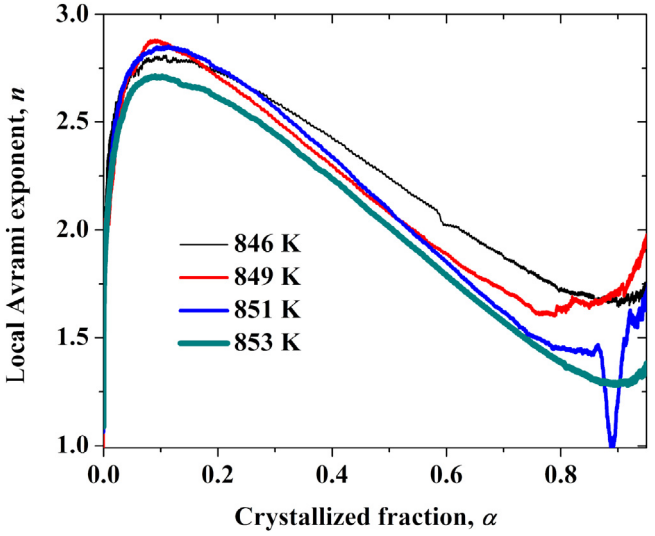

Fig. 10. Variations of the local Avrami exponents ($n(\alpha)$) as a function of the crystallized fraction (α) at the different annealing temperatures for the $Co_{46.45}Fe_{25.55}Ta_8B_{20}$ MG.

annealing temperatures. The figure reveals that the trend of the Avrami exponent variations with the crystallized fraction is similar, regardless of the annealing temperature. At the initial devitrification stages, n increases, reaches its maximum at $\alpha = 0.1$, and subsequently decreases gradually for each annealing temperature. From Fig. 10, the maximum of the n values at the beginning of crystallization lies between 2.7 and 2.9, which indicates a three-dimensional growth with increasing the nucleation rate. A relatively similar Avrami exponent was calculated for the isochronal mode (Fig. 5) but at smaller transformed fractions ($\alpha \leq 0.05$). The increase of α beyond 0.1 (see Fig. 10) is accompanied by a continuous decrease of n up to around 1.5 at the final stages of crystallization, manifesting the reduction of the nucleation rate up to about zero (site saturation) at each annealing temperature. Compared to crystallization in the isochronal regime, in which the site saturation starts around $\alpha = 0.3$ (Fig. 5), it can be deduced that the nucleation of crystals can take place in a significantly larger span during the isothermal heating process. In other words, the JMA model can be applied for a larger extent of crystallization in the isothermal approach in order to determine the kinetics parameters. This effect can be attributed to the more period available for the nucleation of crystals in the isothermal mode, compared to the isochronal one. From Fig. 10, the average values of the Avrami exponent n_{avg} over the entire crystallization range were determined (Table 3). It is observed that the n_{avg} values are relatively similar for all of the annealing temperatures, demonstrating a three-dimensional growth with decreasing the nucleation rate. It is noteworthy that the n_{avg} values are comparable to the average Avrami exponent ($n = 2$) calculated for isochronal crystallization. This effect indicates that the average nucleation or growth rate of the $(Co,Fe)_{21}Ta_2B_6$ crystals are relatively similar in the isochronal and isothermal conditions.

4. Conclusions

The crystallization kinetics of $Co_{46.45}Fe_{25.55}Ta_8B_{20}$ soft magnetic metallic glass with high thermal stability was investigated during isochronal and isothermal annealing treatments. The apparent activation energy of the first crystallization event in the isochronal condition, determined by different approaches consisting of Kissinger, Ozawa, Augis–Bennett and Gao, showed relatively close values. Furthermore, based on the JMA approach, an average Avrami exponent of 2, as the characteristic of three-dimensional diffusion-controlled growth with a decreasing nucleation rate, was calculated for the crystallized fraction less than 0.5 under continuous heating. Under the isochronal condition, the site saturation occurred at the devitrified fraction of about 0.3, and subsequently crystallization proceeded by a NGG process with an exponent of 0.32. It was found that the average Avrami exponents calculated according to the JMA model in the isothermal and isochronal conditions were similar, demonstrating a comparable overall nucleation rate for crystallization under these heating regimes. Compared to the isochronal mode, the JMA analysis indicated that the nucleation process was involved in a significantly larger crystallized fraction in the isothermal annealing experiment.

Acknowledgments

A.H. Taghvaei is grateful to the Iran National Science Foundation (INSF, Grant No: 93005710) for financial support.

References

[1] A. Inoue, C. Suryanarayana, Bulk Metallic Glasses, Boca Raton, New York, 2011.
[2] B.A. Sun, W.H. Wang, The fracture of bulk metallic glasses, Prog. Mater. Sci. 74 (2015) 211–307.
[3] A. Inoue, A. Takeuchi, Recent development and application products of bulk glassy alloys, Acta Mater 59 (2011) 2243–2267.
[4] M.M. Trexler, N.N. Thadhani, Mechanical properties of bulk metallic glasses, Prog. Mater. Sci. 55 (2010) 759–839.
[5] Y.Q. Cheng, E. Ma, Atomic-level structure and structure–property relationship in metallic glasses, Prog. Mater. Sci. 56 (2011) 379–473.
[6] E. Salahinejad, R. Amini, M. Marasi, T. Sritharan, M.J. Hadianfard, The effect of nitrogen on the glass forming ability and micro-hardness of Fe–Cr–Mn–N amorphous alloys prepared by mechanical alloying, Mater. Chem. Phys. 118 (2009) 71–75.
[7] R. Amini, E. Salahinejad, M.J. Hadianfard, M. Marasi, T. Sritharan, Characterization of Fe–Cr–Mn–N amorphous powders with a wide supercooled liquid region developed by mechanical alloying, Mater. Sci. Eng. A 527 (2010) 1135–1142.
[8] R. Amini, E. Salahinejad, E. Askari Bajestani, M.J. Hadianfard, On the general outline of physical properties of amorphous-nanocrystalline Fe–Cr–Mn–N alloy powders prepared by mechanical alloying under nitrogen, J. Alloys Compds 509 (2011) 3252–3256.
[9] C. Yang, Q.R. Cheng, L.H. Liu, Y.H. Li, Y.Y. Li, Effect of minor Cu content on microstructure and mechanical property of NiTiCu bulk alloys fabricated by crystallization of metallic glass powder, Intermetallics 56 (2015) 37–43.
[10] X. Li, H. Kato, K. Yubuta, A. Makino, A. Inoue, Improved plasticity of iron-based high-strength bulk metallic glasses by copper-induced nanocrystallization, J. Non-Cryst. Solids 357 (2011) 3002–3005.
[11] J. Fornell, S. González, E. Rossinyol, S. Suriñach, M.D. Baró, D.V. Louzguine-Luzgin, J.H. Perepezko, J. Sort, A. Inoue, Enhanced mechanical properties due to structural changes induced by devitrification in Fe–Co–B–Si–Nb bulk metallic glass, Acta Mater 58 (2010) 6256–6266.
[12] T. Kubota, A. Makino, A. Inoue, Low core loss of $Fe_{85}Si_2B_8P_4Cu_1$ nanocrystalline alloys with high Bs and B800, J. Alloy. Compd. 509S (2011) S416–S419.
[13] J.E. Gao, H.X. Li, Z.B. Jiao, Y. Wu, Y.H. Chen, T. Yu, Z.P. Lu, Effects of nanocrystal formation on the soft magnetic properties of Fe-based bulk metallic glasses, Apply. Phys. Lett. 99 (2011) 052504–052506.
[14] A.P. Tsai, T. Kamiyama, Y. Kawamura, A. Inoue, T. Masumoto, Formation and precipitation mechanism of nanoscale Al particles in Al-Ni base amorphous alloys, Acta Mater 45 (1997) 1477–1487.
[15] Q. Hu, M.W. Fu, X.R. Zeng, Thermostability and thermoplastic formability of $(Zr_{65}Cu_{17.5}Ni_{10}Al_{7.5})_{100-x}RE_x$ (x = 0.25–3.25, RE: Y, Gd, Tb, Dy, Ho, Er, Tm, Yb, Lu) bulk metallic glasses, Mater. Des. 64 (2014) 301–306.
[16] N. Li, Y. Chen, M.Q. Jiang, D.J. Li, J.J. He, Y. Wu, L. Liu, A thermoplastic forming map of a Zr-based bulk metallic glass, Acta Mater 61 (2013) 1921–1931.
[17] W.A. Johnson, R.F. Mehl, Reaction kinetics in processes of nucleation and growth, Trans. Am. Inst. Min. Metall. Pet. Eng. 135 (1939) 416.
[18] M. Avrami, Kinetics of phase change. I. General theory, J. Chem. Phys. 7 (1939) 1103–1112.
[19] Z. Yuan, X. Chen, B. Wang, Y. Wang, Kinetics study on non-isothermal crystallization of the metallic $Co_{43}Fe_{20}Ta_{5.5}B_{31.5}$ glass, J. Alloys. Compd. 407 (2006) 163–169.
[20] H.E. Kissinger, Reaction kinetics in differential thermal analysis, Anal. Chem. 29 (1957) 1702–1706.
[21] T. Ozawa, Kinetic analysis of derivative curves in thermal analysis, J. Therm. Anal. 2 (1970) 301–324.
[22] J.A. Augis, J.E. Bennett, Calculation of the Avrami parameters for heterogeneous solid state reactions using a modification of the Kissinger method, J. Therm. Anal. 13 (1978) 283–292.
[23] Y.Q. Gao, W. Wang, On the activation energy of crystallization in metallic glasses, J. Non-Cryst. Solids 81 (1986) 129–134.
[24] A.T.W. Kempen, F. Sommer, E.J. Mittemeijer, Determination and interpretation of isothermal and non-isothermal transformation kinetics; the effective activation energies in terms of nucleation and growth, J. Mater. Sci. 37 (2002) 1321–1332.
[25] Q.P. Cao, J.W. Liu, J.F. Li, Y.H. Zhou, X.D. Wang, J.Z. Jiang, Isochronal crystallization kinetics of $Cu_{60}Zr_{20}Ti_{20}$ bulk metallic glass, J. Non-Cryst. Solids 357 (2011) 1182–1187.
[26] J.C. Qiao, J.M. Pelletier, Crystallization kinetics in $Cu_{46}Zr_{45}Al_7Y_2$ bulk metallic glass by differential scanning calorimetry (DSC), J. Non-Cryst. Solids 357 (2011) 2590–2594.
[27] Y.J. Yang, D.W. Xing, J. Shen, J.F. Sun, S.D. Wei, H.J. He, D.G. McCartney, Crystallization kinetics of a bulk amorphous Cu–Ti–Zr–Ni alloy investigated by differential scanning calorimetry, J. Alloys. Compd. 415 (2006) 106–110.
[28] A.H. Taghvaei, J. Bednarčik, J. Eckert, Atomic structure and thermal behavior of $(Co_{0.65},Fe_{0.35})_{72}Ta_8B_{20}$ metallic glass with excellent soft magnetic properties, Intermetallics 69 (2016) 21–27.
[29] N. Clavaguera, M. Clavaguera-Mora, M. Fontana, Accuracy in the experimental calorimetric study of the crystallization kinetics and predictive transformation diagrams: application to a Ga-Te amorphous alloy, J. Mater. Res. 13 (1998) 744–753.
[30] Y.X. Zhuang, T.F. Duan, H.Y. Shi, Calorimetric study of non-isothermal crystallization kinetics of $Zr_{60}Cu_{20}Al_{10}Ni_{10}$ bulk metallic glass, J. Alloy. Compd. 509 (2011) 9019–9025.
[31] J.S. Blázquez, C.F. Conde, A. Conde, Non-isothermal approach to isokinetic crystallization processes: application to the nanocrystallization of HITPERM alloys, Acta Mater 53 (2005) 2305–2311.
[32] J.W. Christian, The Theory of Transformation in Metals and Alloys, Pergamon

Press, Oxford, 1975.
[33] A.H. Taghvaei, M. Stoica, K. Song, K. Janghorban, J. Eckert, Crystallization kinetics of Co40Fe22Ta8B30 glassy alloy with high thermal stability and soft magnetic properties, J. Alloy. Compd. 605 (2014) 199–207.
[34] K. Matusita, T. Komatsu, R. Yokota, Kinetics of non-isothermal crystallization process and activation energy for crystal growth in amorphous materials, J. Mater. Sci. 19 (1984) 291–296.
[35] S. Ranganathan, M.V. Heimendahl, The three activation energies with isothermal transformations: applications to metallic glasses, J. Mater. Sci. 16 (1981) 2401–2404.
[36] J. Torrens-Serra, S. Venkataraman, M. Stoica, U. Kuehn, S. Roth, J. Eckert, Non-Isothermal kinetic analysis of the crystallization of metallic glasses using the master curve method, Materials 4 (2011) 2231–2243.
[37] M. Avrami, Kinetics of phase change. II. Transformation-time relations for random distribution of nuclei, J. Chem. Phys. 8 (1940) 212–224.
[38] Z.Z. Yuan, X.D. Chen, B.X. Wang, Y.J. Wang, Kinetics study on non-isothermal crystallization of the metallic $Co_{43}Fe_{20}Ta_{5.5}B_{31.5}$ glass, J. Alloys. Compd. 407 (2006) 163–169.
[39] B.D. Cullity, Elements of X-ray Diffraction, Addison Wesley Pub. Co. Inc., London, 1956.